Expanding Limit of Minimum Sampling Time Using Auxiliary Vectors for PMSM Drives with Single DC-Link Current Sensor

Yuge Song, Jiadong Lu, *Senior Member, IEEE*, Yihua Hu, *Senior Member, IEEE,* Wei Zhang, Yue Su, Xuyang Wu, and Jinglin Liu, *Member, IEEE*

Abstract—**Phase current reconstruction (PCR) strategy can improve the fault tolerance of permanent magnet synchronous motor (PMSM) drives. The PCR precision is largely affected by the unmeasurable zones and time-sharing sampling errors. The upper limit (T_{limit}) of PCR allowable range can reflect the requirement of different PCR methods for the minimum sampling time (T_{min}). With a longer T_{limit}, there is sufficient time for sampling, even if T_{limit} is halved due to the symmetrical waveform. Therefore, the extension of T_{limit} is the key to eliminate the unmeasurable zones and time-sharing sampling errors. In this paper, a method to increase T_{limit} is proposed, which introduces the suitable auxiliary vectors (AVs) in different regions to extend the duration time of the sampling vectors. With the help of a longer T_{limit} ($12.5\%T_s$), it's possible to eliminate all the unmeasurable zones and time-sharing sampling errors, relieve the pressure on the hardware of current loop, improve the sampling accuracy, and facilitate the reliable operation of the drive. Besides, the switching action times of IGBTs can be reduced by about one-third in the high modulation area. The proposed method is finally proved to accurately reconstruct the phase currents by the experimental results on the PMSM prototype.**

Index Terms—**Permanent magnet synchronous motor (PMSM), phase current reconstruction (PCR), minimum sampling time (T_{min}), auxiliary voltage vectors (AVs), pulse width modulation (PWM).**

I. INTRODUCTION

PERMANENT magnet synchronous motor (PMSM) has been widely used in industrial applications because of its high reliability, power/torque density, and efficiency [1]-[9]. Conventionally, two current sensors are installed to measure the phase currents, and a DC-link current sensor is installed for

Y. Song, J. Lu, W. Zhang, Y. Su, X. Wu and J. Liu are with the School of Automation, Northwestern Polytechnical University (NWPU), Xi'an 710129, China. (E-mail: songyuge@mail.nwpu.edu.cn, j.d.lu@nwpu.edu.cn, zhangweichn@mail.nwpu.edu.cn, suyue2020@mail.nwpu.edu.cn, wuxuyang@mail.nwpu.edu.cn, jinglinl@nwpu.edu.cn).

Y. Hu is with the Department of Electronic Engineering, University of York, York YO10 5DD, U.K. (E-mail: yihua.hu@york.ac.uk).

protection. For the propose of improving the fault tolerance and reducing cost, the phase current reconstruction (PCR) strategy with a DC-link current sensor has been studied.

In the PCR technology, feedback currents are reconstructed by extracting the DC-link current when sampling vectors (SVs) are acting. However, there are mainly two factors that cause degradation of the reconstruction currents accuracy in this extraction process.

The first factor is that the actual DC-link current cannot follow the applied SV as immediately as the ideal one, which is illustrated in the middle of Fig. 1(a). To sample effectively, the duration time of SVs must exceed a minimum sampling time (T_{min}) [13] that depends on the hardware of the current loop, which can be expressed as

$$T_{\text{min}} = T_{\text{dead}} + T_{\text{delay}} + T_{\text{sett}} + T_{\text{AD}} \tag{1}$$

where T_{dead} is the dead time for the pass-through protection which is provided by the driver board, T_{delay} is the delay time of IGBTs to turn-on or turn-off, T_{sett} is the settling time which is mainly determined by the motor inductance and also affected by the sampling process, and T_{AD} is the sum of sampling time and A/D conversion time which depends on the controller.

In the maximum modulation circle, the areas that fail to be accurately reconstructed are called unmeasurable zones. The upper limit of PCR allowable range is defined as T_{limit}, which can reflect the requirement of different PCR methods for T_{min}. T_{min} must be less than T_{limit}, otherwise, the modulation area will be reduced. Therefore, both decreasing T_{min} and increasing T_{limit} can avoid unmeasurable zones. The limit factors of decreasing T_{min} are shown in Fig. 1(a). First, the pass-through protection time of the driver board requires a strict design for decreasing T_{dead}, but insufficient protection time might cause a short circuit of the inverter. Then, the inverter must have higher performance requirements to reduce T_{delay}, such as the faster turn-on and turn-off time. Moreover, to shorten T_{sett}, a higher bandwidth current sensor is required to measure current signals, and the current sampling board is also designed to shorten delay time, accelerate response, and reduce interference. Finally, to decrease T_{AD}, the performance of controller needs to be improved, and the sampling time should be shortened. As is mentioned above, shrinking T_{min} cannot eliminate all the unmeasurable zones but increases the cost and design difficulty of the hardware. Therefore, enlarging T_{limit} might be a useful method to eliminate the unmeasurable zones.

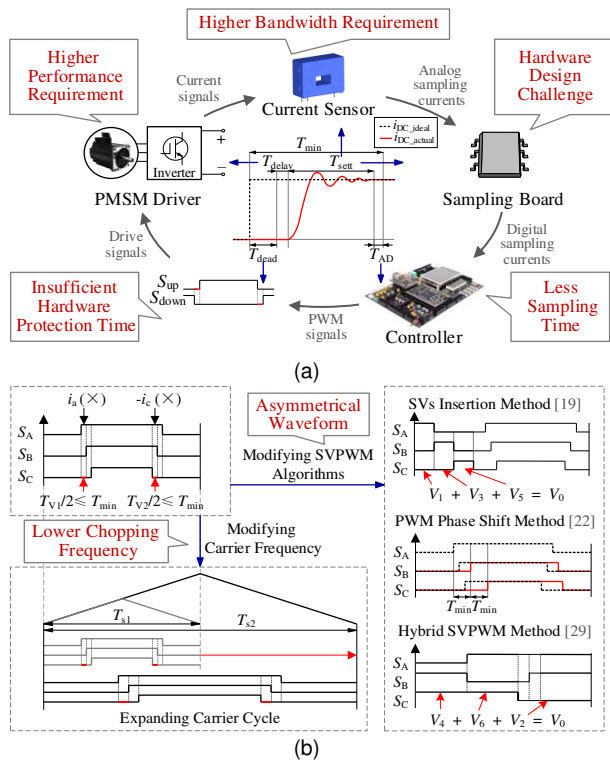To find a method to expand T_{limit}, various advanced PCR

Fig. 1. Eliminating unmeasurable zones by hardware and software: (a) limit factors of decreasing T_{min}, and (b) methods of increasing T_{limit}.

methods [10]-[29] are discussed. By using the different observers, the current in the unmeasurable zones can be estimated in literature [10]-[12]. However, this method fails in the low modulation area due to the lack of two-phase current information at the same time, and the unmeasurable zones still exist in the maximum modulation circle. To accurately measure rather than estimate the current in unmeasurable zones, various advanced methods [13]-[29] have been proposed, which can be generally divided into two categories according to the location of the current sensor. In the first method, the current sensor is uninstalled at the DC-link side [13]-[18], and the DC-link current corresponding to the voltage vector must be changed. Although changing the position of the sensor is flexible and simple, the unmeasurable zones may just be transferred to other positions in the maximum modulation circle, i.e., the unmeasurable zones might not be eliminated and T_{limit} is equal to zero. To turn things around, the second method is put forward to modify the seven-segment space vector pulse width modulation (SVPWM) algorithm with a single DC-link current sensor [19]-[29], where three typical examples are shown in Fig. 1(b). By inserting three SVs that are added up to zero, literature [19] and [20] eliminate the unmeasurable zones in the maximum modulation circle, and T_{limit} probably does not exceed $4\%T_s$. Works [21]-[26] move the pulse width modulation (PWM) waveforms without changing the duty cycle to obtain enough sampling time. These methods also have different and strict constraints on T_{min}. And T_{limit} is stipulated in literature [22], which is $3.5\%T_s$ approximately. The hybrid SVPWM methods are raised in [27]-[29], which compensate for the duration time of SVs by introducing new vectors. In [28], a method adopts correspondingly comprehensive strategies for reference voltage vectors (V_{ref}). However, there may still be some stubborn

unmeasurable zones in the low modulation area, which leads to inaccurate sampling. In [29], the problem of unmeasurable zones is addressed by an independent current reconstruction strategy without null switching states, leading to an independence of PCR. But the modulation area may be reduced as T_{min} increases. Therefore, modifying the algorithm seems to be the valid way to increase T_{limit}.

The second factor is that the three-phase currents cannot be simultaneously obtained with one single current sensor, which introduces the time-sharing sampling errors [30]. These errors cause current waveform fluctuations similar to offset jitter, resulting in the waveform distortion shown in [31]. Unfortunately, the time-sharing sampling errors cannot be compensated by a constant value, because they are related to the current slope, the voltage vector, and its duration time. Assuming that the current slopes are identical under the same vector in the same PWM cycle [36], the symmetrical sampling method using symmetrical PWM waves can eliminate these errors simply and effectively. However, owing to the harsh T_{limit}, it is difficult to generate symmetrical PWM waves while ensuring sufficient duration time for SV. The current prediction method is often selected in [30]-[37], even if the variable parameters affect the prediction results and the computational burden is heavy.

Based on the above analysis, the extension of T_{limit} is the key to eliminate all the unmeasurable zones in the maximum modulation circle and time-sharing sampling errors by the symmetrical sampling method. Fig. 1(b) shows the cause of unmeasurable zones in the low modulation of sector I and the methods of increasing T_{limit}. T_{limit} is determined by the algorithm in the controller, including PCR algorithm and carrier frequency. Although T_{limit} can be enlarged by modifying the SVPWM algorithm in the above-mentioned method, T_{limit} cannot exceed $4\%T_s$ without affecting the maximum modulation circle. The harsh T_{limit} makes it difficult to generate symmetrical PWM waves. Meanwhile, to ensure the reliable current sampling, T_{min} is set as 5 us [15]. With the carrier frequency of 10kHz, there are still unmeasurable zones within the maximum modulation circle. Decreasing carrier frequency is another method to expand T_{limit}. When T_{limit} is not equal to zero, with the decrease of the carrier frequency, T_{limit} increases appropriately, but the waveform is distorted and the operation of PMSM is affected. Thus, it is necessary to bring forward a method with a longer T_{limit}. As well as reducing the burden on the hardware circuit, a simple symmetrical sampling method can also be used to eliminate the time-sharing sampling errors.

Aiming at expanding T_{limit}, a method is proposed in this paper, which introduces different auxiliary vectors (AVs) for prolonging the duration time of SVs. With the help of a larger T_{limit}, it is possible to generate symmetrical PWM waves, thereby simply eliminating time-sharing sampling errors by the symmetrical sampling method. Moreover, a longer T_{limit} ($12.5\%T_s$) allows to relieve the pressure on the hardware of current loop, produce a more stable current waveform during sampling, and improve the sampling accuracy by multiple sampling. Besides, the switching times of IGBTs can be reduced by about one-third in the high modulation area.

This article is organized as follows. In Section II, the features

of AVs in the existing PCR method are analyzed. Based on the analysis, the proposed PCR method with different AVs is presented in Section III. The calculation of T_{limit} for the proposed method is shown in Section IV. In Section V, experimental results are presented. Conclusions are given finally.

II. FEATURES OF AVs IN EXISTING PCR METHOD

A. Principle of Unmeasurable Zones Elimination

Eight basic voltage vectors of the inverter are defined as two zero vectors: V_{000} (V_0), V_{111} (V_7), and six active vectors: V_{100} (V_1), V_{110} (V_2), V_{010} (V_3), V_{011} (V_4), V_{001} (V_5), V_{101} (V_6). The DC-link current (i_{DC}) is related to the three-phase currents (i_a, i_b, and i_c) in different switching states [23]. The sum of the three-phase currents is 0, so at least two SVs are indispensable for obtaining the three-phase currents with a DC-link current sensor in each PWM cycle. Furthermore, it is necessary to introduce one or more basic vectors to assist in the synthesis of V_{ref}.

Taking Fig. 1(b) as an example, each segment duration time of SVs (T_{V1}, T_{V2}) is shorter than T_{min}. The reconstruction currents (i_a, i_b) cannot be accurately sampled, therefore, modifying the SVPWM algorithm is proposed to eliminate the unmeasurable zones. Three typical examples in Fig. 1(b) are analyzed in detail. Literature [19] introduced three SVs whose sum is 0, and the three-phase currents are thus obtained. Two sets of vector pairs V_1 and V_4, V_2 and V_5 with opposite directions are used to replaced part of the zero vectors in [22]. Literature [29] uses V_2, V_4 and V_6 to replace all zero vectors. In the maximum modulation area, the duration time of shortest SV is equal to T_{limit}, so extending the duration time of SVs is the key to extend T_{limit}. The above three typical examples essentially replace part or all of the zero vectors by adding active vectors to extend T_{limit}. In this paper, the active vectors are used as AVs to replace all the zero vectors, meanwhile, the two adjacent vectors of each sector are specified as SVs, which can guarantee the longest duration time of SVs.

B. Influence of AVs on Output Vector Area

The introduction of AVs is regarded as an important method to reduce the unmeasurable zones, i.e., superimposing different AVs can eliminate the unmeasurable zones of a specific part. To expand T_{limit}, the features of AVs are studied. The addition of different AVs has a special effect on V_S generated by SVs. If the angle between AV and V_S is less than $\pi/2$, the length of V_S will increase theoretically, and the angle will shift to the boundary of the sector. Similarly, if this angle is between $\pi/2$ and π, the length of V_S will shorten and the angle will shift to the boundary or low modulation area.

Combining the above analysis, the output vector area after introducing different AVs in sector I is represented in Fig. 2, where SVs adjacent to sector I are V_1 and V_2. Sector I is divided into two parts by its angle bisector l_0, and the angle between the upper part and V_3 is less than $\pi/2$. Under the influence of V_3, the output vector area expands in the boundary area of high modulation, as shown in Fig. 2(a). The angle between the upper part and V_4 is more than $\pi/2$. Under the influence of V_4, the output vector area expands towards the boundary area of low modulation, as shown in Fig. 2(b). Similarly, V_5 and V_6 have the same effect as above on the lower part of the area.

Ideally, the output vector area is the largest. And as T_{min}
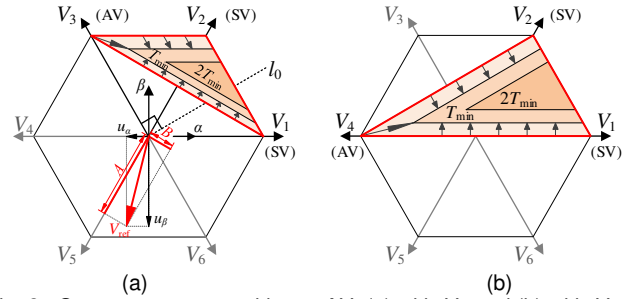

Fig. 2. Output vector area with one AV: (a) with V_3, and (b) with V_4.

increases, the area shrinks. It can be clearly illustrated from Fig. 2. When there is a fixed T_{min}, the output vector area is reduced by a certain percentage. To generate symmetrical PWM waves, each duration time of SVs must be greater than $2T_{\text{min}}$. With this limit, the output vector area is further reduced. However, it can still guarantee that there remains no unmeasurable zone with the increase of T_{min} in some specific areas. In order to expand T_{limit}, the sector is divided into different regions in the proposed method, and the different AV is used in the different region.

However, as shown in Fig. 2(b), as long as T_{min} exists, there must be unmeasurable zones in the low modulation area. Therefore, two AVs (V_4, V_5) are introduced at the same time, and an output area appears, as shown in Fig. 3(a). Both form two vectors paired with SVs in the opposite directions, i.e., (V_1, V_4) and (V_2, V_5). It is stipulated that T_{V1}, T_{V2}, T_{V4}, and T_{V5} represent the duration of V_1, V_2, V_4, and V_5. However, the output vector is only related to the values of T_{V1} minus T_{V4} and T_{V2} minus T_{V5}, resulting in a non-unique synthesis method. To solve this problem, the duration of two vector pairs is specified by $0.5T_s$. And the output voltage area is shown in Fig. 3(b). The constraints can achieve a more balanced duration time of SVs and AVs, which can benefit the stability of motor control and ease the computational burden. Meanwhile, as long as T_{min} does not exceed $25\%T_s$, it can be guaranteed that there is no unmeasurable zone in the low modulation area, and the addition of restriction conditions has no effect on this range.
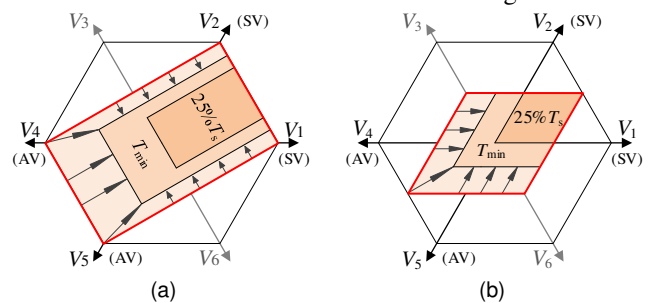
Fig. 3. Output vector area with two AVs: (a) without restriction, and (b) duration time of two vector pairs is equal.

C. Feature of Each Sector

According to the above analysis, each sector must be subdivided, which makes the algorithm more complicated. Fortunately, sector s can coincide with sector I by rotating

TABLE I
RESULTS OF CONVERT V_{REF} TO SECTOR I.

Sector	A	B
I or IV	$\|a\|$	$\|b\|$
II or V	$((-1)^s a + 3k\|b\|)/2$	$((-1)^{s+1} 3ka + \|b\|)/2$
III or VI	$(\|a\| + 3k\|b\|)/2$	$(3k\|a\| - \|b\|)/2$
$k = \tan \pi/6$		

$(s-1)\pi/3$ clockwise. Therefore, any V_{ref} can be equivalent to V_{ref}' in sector I for unified calculation. The equivalent projected values A and B for converting V_{ref} to sector I are given in TABLE I, where $|a|$ and $|b|$ are the unit lengths of u_α and u_β, and s represents the number of the sector. For example, when V_{ref} is located in sector V, u_α, u_β, A and B are legibly shown in Fig. 2(a). After the unified calculation is completed, the required V_{ref} can be generated according to the sector number s.

III. PROPOSED PCR SCHEME WITH DIFFERENT AVS

A harsh T_{limit} raises the higher performance requirements on PMSM drive systems. Meanwhile, T_{limit} limits the generation of symmetrical PWM waves, which makes it unfeasible to use the simple symmetrical sampling method to eliminate the time-sharing sampling errors. To extend T_{limit}, a method with different AVs is proposed to divide each sector into five regions, which is described in detail in this Section.

A. Region Division Method

Based on the analysis of the position characteristics and effects of the six active vectors in Section II, sector I is divided, which is introduced in Fig. 4(a). V_1 and V_2 are called SVs, and V_3 to V_6 are named AVs. The AVs of region 1 are V_4 and V_5, and V_{ref}' in region 2 or 3 can be synthesized by introducing V_5 or V_4. Likewise, V_6 or V_3 are used to synthesize V_{ref}' of region 4 or 5.
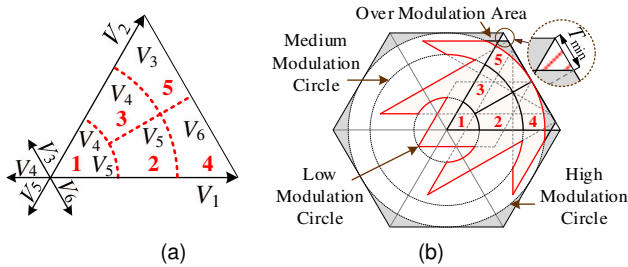

Fig. 4. Redivision method of sector I: (a) defined five regions, and (b) sum of output voltage areas of five regions.

The generation of symmetrical PWM wave leads to the reduction of T_{limit}. To extend T_{limit} as much as possible while generating symmetrical waves, a one-time SV (OSV) is placed in the middle of the waveform, and a two-time SV (TSV) is divided into two parts on both sides of OSV. AV, OSV, TSV corresponding to regions 1 to 5 are illustrated in TABLE II.

TABLE II
BASIC VECTOR USED IN FIVE REGIONS FOR SECTOR I.

Basic Vectors	Region	AV(s)	OSV	TSV
V_1, V_2 V_4, V_5	1	V_4, V_5	V_1 / V_2	V_1 / V_2
	2	V_5	V_2	V_1
	3	V_4	V_1	V_2
V_1, V_2 V_3, V_6	4	V_6	V_2	V_1
	5	V_3	V_1	V_2

To ensure the accuracy of sampling, the duration time of OSV and TSV must be longer than T_{min} and $2T_{\text{min}}$ respectively. And the total durations of the vectors are equal to T_s. According to Part B of Section II, the durations of two vector pairs are specified by $0.5T_s$. T_{V1} and T_{V2} are also required to surpass $2T_{\text{min}}$ simultaneously to produce a symmetrical output voltage area for dealing with their nondistinctive correspondence to OSV and

TSV. The sum of output voltage areas of five regions is displayed in Fig. 4(b).

Generally, to ensure the smooth operation of the motor, V_{ref} falls into the maximum modulation circle, i.e., the inscribed circle of the regular hexagon. Therefore, if these two triangular areas are outside the maximum modulation circle, the stable operation of the motor cannot be affected.

The modulation area is divided into three parts, and the boundaries from the inside to the outside are named as low, medium, and high modulation circles, as shown in Fig. 4(b), where the high modulation circle is identical with the maximum one. In Fig. 5, the radius of the circle in low, medium, and high modulation areas are $|Oa|$, $|Ob|$, and $|Oc|$ respectively, and a Cartesian coordinate system is created.
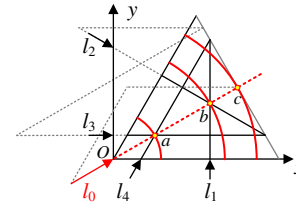

Fig. 5. Calculation of region division boundaries.

The equation of the lines l_0, l_1, l_2, l_3 and l_4 can be easily obtained as follows:

$$l_0 : y = x / \sqrt{3} \tag{2}$$

$$l_1 : x = T_s / 2 + T_{\text{min}} \tag{3}$$

$$l_2 : y = -\sqrt{3}x / 3 + \sqrt{3}T_s / 3 + 2\sqrt{3}T_{\text{min}} / 3 \tag{4}$$

$$l_3 : y = \sqrt{3}T_{\text{min}} \tag{5}$$

$$l_4 : y = \sqrt{3}x - 2\sqrt{3}T_{\text{min}} \tag{6}$$

Combining the above equations of (3) to (6), the coordinates of points a and b can be obtained. The values of $|Oa|$, $|Ob|$ and $|Oc|$ can be obtained as follows:

$$\begin{cases} |Oa| = 2\sqrt{3}T_{\text{min}} \\ |Ob| = \sqrt{3}T_s / 3 + 2\sqrt{3}T_{\text{min}} / 3 \\ |Oc| = \sqrt{3}T_s / 2 \end{cases} \tag{7}$$

In addition, regions 2 and 3, regions 4 and 5 are separated by l_0. R represents the product of T_s and the unit value of V_{ref}'. V_{ref}' falls into region 1 when R is shorter than $|Oa|$; it falls into region 2 or 3 as long as R is longer than $|Oa|$ but shorter than $|Ob|$. If $A>\sqrt{3}B$, it falls into region 2, otherwise, it falls into region 3; Suppose that R is longer than $|Ob|$, V_{ref}' falls into region 4 or 5. If $A>\sqrt{3}B$, it falls into region 4, otherwise, it falls into region 5.

B. Duration Time of Applied Vectors

There are three constraints to decompose V_{ref}':
1) The sum of vectors in the horizontal direction is equal to the horizontal projection of V_{ref}'.
2) The sum of vectors in the vertical direction is equal to the vertical projection of V_{ref}'.
3) The sum of the durations of vectors are equal to T_s.

The durations of OSV, TSV and AV in region 2 to 5 can be easily calculated with the above three conditions, which are required to generate the expected PWM waveform. The calculation results are shown in TABLE III.

In region 1, there are four active vectors used. In addition to the above three conditions, it is also necessary to specify that the durations of the two vector pairs are $0.5T_s$. Therefore, the durations of the four vectors V_1, V_2, V_4 and V_5 are calculated as:

$$\begin{cases} T_{V1} = \left(1/4 + A/2 - \sqrt{3}B/6\right)T_s \\ T_{V2} = \left(1/4 + \sqrt{3}B/3\right)T_s \\ T_{V4} = \left(1/4 - A/2 + \sqrt{3}B/6\right)T_s \\ T_{V5} = \left(1/4 - \sqrt{3}B/3\right)T_s \end{cases} \quad (8)$$

C. PWM Synthesis Method

To obtain a unique symmetrical PWM waveform, the following constraints must be satisfied. OSV must be placed in the middle of each PWM cycle, and TSV must be bisected and placed on both sides of OSV. In region 2 to 5, AV is bisected at both ends of the PWM cycle. Besides, the AVs are placed to ensure the minimum switching times of IGBTs in each PWM cycle of region 1.

After calculating the durations of TSVs and AVs, T_1, T_2 and T_3 can be obtained, which can represent the transition time of the PWM signals. There are two AVs and three turning points in region 1, where T_{V4} and $T_{V5}+T_{V4}$ are defined as T_1 and T_2, respectively. And the duration time of the third vector can be calculated by $T_3 = T_2 + T_s/2 - T_1$, where T_1, T_2 and T_3 are marked in Fig. 6(a). From region 2 to 5, T_1 is equal to 0, T_2 is the duration time of AV, and T_3 is defined as the total durations of AV and TSV in TABLE III, where T_2 and T_3 are marked in Fig. 6(b).

TABLE III
DURATION TIME OF TSVS AND AVS IN SECTOR I.

Region	Duration time of TSV	Duration time of AV(s)
1	$T_{V1} = 0.5T_s(0.5+A-kB)$	$T_{V5} = 0.5T_s(0.5-2kB)$ $T_{V4} = 0.5T_s(0.5-A+kB)$
2	$T_{V1} = T_s(A-kB)$	$T_{V5} = 0.5T_s(1-A-kB)$
3	$T_{V2} = 2T_s kB$	$T_{V4} = 0.5T_s(1-A-kB)$
4	$T_{V1} = T_s(-1+2A)$	$T_{V6} = T_s(1-A-kB)$
5	$T_{V2} = T_s(-1+A+3kB)$	$T_{V3} = T_s(1-A-kB)$
	$k = \tan \pi/6$	

According to the abovementioned requirements, when $T_s = 100\mu s$, $T_{min} = 10\mu s$, V_{ref}' enters unmeasurable zones of five regions by the seven-segment SVPWM method. Using the proposed method, the PWM signals of V_{ref}' in five regions are shown in Fig. 6(a)-(e), which eliminate previously unmeasurable zones. Through the waveform relationship of each sector in TABLE IV, combined with the number of the sector, the PWM waveform can be converted to the sector where V_{ref} falls, where the negative sign (−) represents the complementary waveform and x represents the number of regions.

D. Sampling Methods

Two-phase currents are reconstructed and the third phase current is obtained indirectly through calculation in this method. Three sampling points are required in one PWM cycle, including two symmetrical sampling points under the duration time of TSV, and a midpoint under the duration time of OSV. The effects of random errors can be mitigated by continuous sampling m ($m>1$) times at each sampling point. Suppose the carrier frequency is f_c, and the sampling frequency is $3mf_c$. The

TABLE IV
PWM WAVEFORM RELATIONSHIP BETWEEN SECTOR I AND REST OF SECTORS.

Sector PWM	I	II	III	IV	V	VI
1	S_{xA}	$-S_{xB}$	S_{xC}	$-S_{xA}$	S_{xB}	$-S_{xC}$
2	S_{xB}	$-S_{xC}$	S_{xA}	$-S_{xB}$	S_{xC}	$-S_{xA}$
3	S_{xC}	$-S_{xA}$	S_{xB}	$-S_{xC}$	S_{xA}	$-S_{xB}$

time-sharing sampling errors could be eliminated by generating the symmetrical PWM waves and replacing the current at the intermediate moment with the average current under the symmetrical duration of TSV. The location and information of the current sampling points are explicitly shown in Fig. 6. Although the symmetrical sampling points change with the values of T_2 and T_3, the calculation method of PWM comparison value is simple and fixed, i.e., $(T_2+T_3)/2$.

In Part C of Section II, to convert V_{ref} to V_{ref}', sector s can coincide with sector I by rotating $(s-1)\pi/3$ clockwise. Therefore, to converse V_{ref}' back to V_{ref}, SVs need to rotate counter clockwise by $(s-1)\pi/3$. For example, when V_{ref} is located in region 3 of sector II, OSV (i_a) and TSV ($-i_c$) need to rotate $\pi/3$ counter clockwise, corresponding to $-i_c$ and i_b respectively.
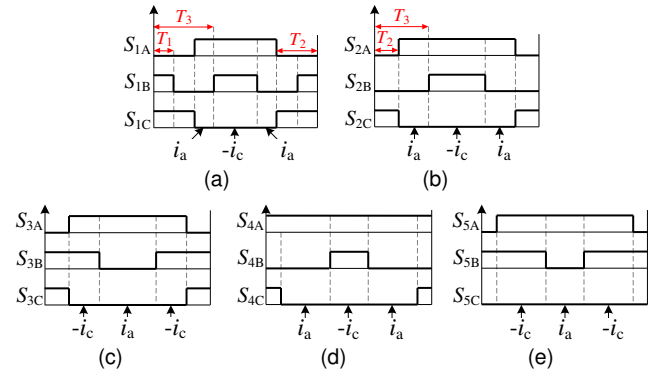

Fig. 6. PWM synthesis strategy and current sampling points in sector I: (a) region 1, (b) region 2, (c) region 3, (d) region 4, and (e) region 5.

IV. CALCULATION OF T_{LIMIT}, FLOWCHART AND DISCUSSION FOR PROPOSED PCR METHOD

A. Calculation of T_{limit}

In the proposed method with different AVs, T_{min} must be less than T_{limit} as well, otherwise, some unmeasurable zones will form in the modulation area. Without reducing the modulation area, it is critical to calculating T_{limit}.

The points e, f and g are the intersections of lines l_6, l_7 and l_8 with l_9, and point d is the intersection of lines l_5 and y-axis, which are all marked out in Fig. 7(a).
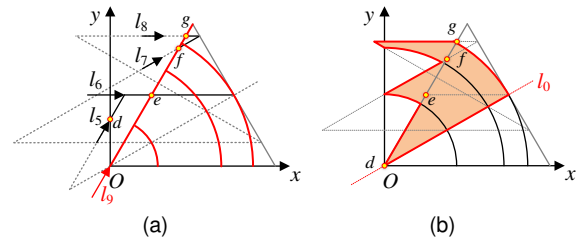

Fig. 7. Range of T_{min}: (a) calculation of T_{limit}, and (b) output voltage areas of maximum T_{limit}.

Establishing the coordinate system as illustrated, the equations of l_5 to l_9 are expressed as follows:

$$l_5 : y = \sqrt{3}x + \sqrt{3}T_s/2 - 4\sqrt{3}T_{min} \qquad (9)$$

$$l_6 : y = \sqrt{3}T_s/4 \qquad (10)$$

$$l_7 : y = \sqrt{3}x/3 + \sqrt{3}T_s/3 - 2\sqrt{3}T_{min}/3 \qquad (11)$$

$$l_8 : y = \sqrt{3}T_s/2 - \sqrt{3}T_{min}/2 \qquad (12)$$

$$l_9 : y = \sqrt{3}x \qquad (13)$$

It is easy to access the coordinates of points d, e and f by combining formulas (9) to (12) with formula (13), and the values of $|Od|$, $|Oe|$, $|Of|$, $|Og|$ can be obtained as follows:

$$\begin{cases} |Od| = \sqrt{3}T_s/2 - 4\sqrt{3}T_{min} \\ |Oe| = T_s/2 \\ |Of| = T_s - 2T_{min} \\ |Og| = T_s - T_{min} \end{cases} \qquad (14)$$

There is no newly-formed unmeasurable zone as long as the length of $|Oe|$, $|Of|$ and $|Og|$ are longer than $|Oa|$, $|Ob|$ and $|Oc|$ respectively and the line l_5 is invariably above the line l_9, i.e., $|Oe|$, $|Of|$, $|Og|$ are longer than $|Oa|$, $|Ob|$, $|Oc|$ respectively, and $|Od|$ is greater than 0. According to the above four constraints, the value of T_{limit}/T_s is 0.125 by calculation. Therefore, when T_s is fixed and T_{min} is less than T_{limit}, i.e., $12.5\%T_s$, there is no unmeasurable zone in the maximum modulation circle, as shown in Fig. 7(b). Meanwhile, a larger T_{limit} brings the following benefits to the PMSM drive system:
1) Higher accuracy of the current sampling information.
2) Higher allowable PWM switching frequency.
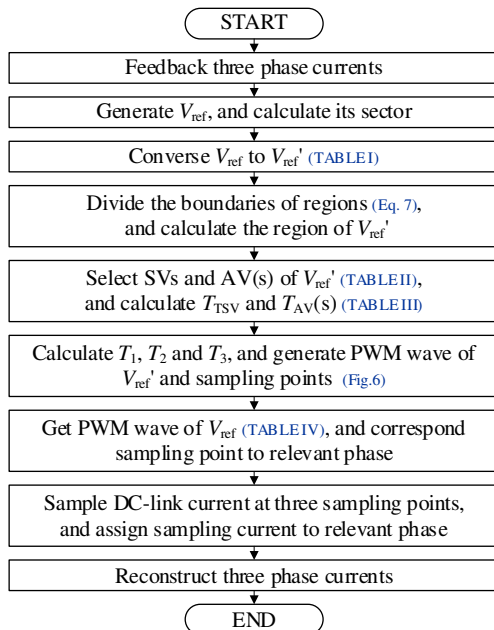3) Lower hardware requirements of the current loop.

START

Feedback three phase currents

Generate V_{ref}, and calculate its sector

Converse V_{ref} to V_{ref}' (TABLE I)

Divide the boundaries of regions (Eq. 7), and calculate the region of V_{ref}'

Select SVs and AV(s) of V_{ref}' (TABLE II), and calculate T_{TSV} and T_{AV}(s) (TABLE III)

Calculate T_1, T_2 and T_3, and generate PWM wave of V_{ref}' and sampling points (Fig.6)

Get PWM wave of V_{ref} (TABLE IV), and correspond sampling point to relevant phase

Sample DC-link current at three sampling points, and assign sampling current to relevant phase

Reconstruct three phase currents

END

Fig. 8. Flowchart of proposed PCR scheme with different AVs.

B. Flowchart for Extracting Phase Currents

The specific steps of the proposed method are clarified in Section III. To clearly illustrate the proposed method, the flowchart to reconstruct the phase currents from dc-link current is shown in Fig. 8.

C. Discussion

1) Switching frequency of inverter

The switching frequency of inverter is described by the upper bridge arm IGBT switching frequency. Each branch has a different switching frequency, depending on the position of V_{ref}. Compared with the seven-segment SVPWM method, one of the three branches switches twice in one PWM cycle of low modulation area, and one branch does not switch in one PWM cycle of high modulation area. Besides, when the sector or region changes, the switching state of a branch may get changed, leading to an increase in the number of switches. The number of additional switches in each branch is related to the speed and modulation area of the motor. The power frequency of motor is $f=np/60$, where n is the motor speed, and p is the number of motor pole pairs. In one electrical period, each branch is switched one, three and five extra times in low, medium, and high modulation areas, respectively. The switching frequencies of three modulation areas are shown in the TABLE V.

TABLE V
SWITCHING FREQUENCIES OF DIFFERENT MODULATION AREAS.

Modulation Areas	Proposed Method
Low	$4f_c/3 + np/60$
Medium	$f_c + np/20$
High	$2f_c/3 + np/12$

Compared with the traditional method, the switching times of IGBTs increase a lot in low modulation area. Since the motor system is usually designed to work in medium or high modulation area, this algorithm is acceptable.

2) Current ripple in capacitor

The current ripple in the capacitor can be reflected by the DC-link current. In the seven-segment SVPWM method, the DC-link current is zero under the duration time of V_0 and V_7. Especially in the low modulation area (longer action time of zero vector), the DC-link current ripple is small. However, the zero vector of the proposed method is synthesized through the active vectors. The currents are opposite to each other when the vectors act in opposite directions, therefore, a large DC-link current fluctuation must be generated with the long duration time of zero vector compared with the traditional method.

V. EXPERIMENTAL RESULTS

To validate the correctness and effectiveness of the proposed PCR scheme with different AVs, an experiment platform is set up, which is shown in Fig. 9. In Fig. 9(a), the power source component is supplied by the AC grid through an isolated transformer and then converted to the DC voltage source (220 V) by using a rectifier. The driver is supplied with a rectifier and a DC-link capacitor. A controller, a sampling board, an inverter, and a drive board are used in the control platform to complete the closed-loop control of the motor drive. The controller (DSP TMS320F28379D) receives the feedback information from the sampling board and resolver decoder, and produces drive signals to the drive boards of the inverter. The DC-link current sensor (LA 25-P) is installed on the sampling board. The drive unit adopts the Infineon IGBT module (FS100R12KT4), which generates the same switching frequency (10 kHz) as that by the PWM carrier. PMSM in the experiment with a resolver can provide the position signal of the rotor, and is loaded by another

motor, with its main parameters given in TABLE VI. Meanwhile, the experimental platform architecture is shown in Fig. 9(b), where the oscilloscope measures the signals from DAC, drive board, current clamps, and torque sensor. The DSP is used to obtain the DAC signals, which can produce three DACs at the same time. The output signal of DAC and the input signal of the oscilloscope in Fig. 9(b) are just for illustration, and the output of different signals depends on different experiments.

Fig. 10 shows the PWM signals of different sectors of each modulation area. The information of sector and region are marked in Fig. 10, and S_A, S_B, and S_C are the signals that control the action of the upper power switches of the three bridge arms. Fig. 10(a) shows the PWM signals when the V_{ref} falls into the low modulation area (x=1). One cycle of each sector is extracted and amplified to verify the correctness of the PWM signals. Fig. 10(b) shows the PWM signals in the middle vector area (x=2 or 3). Similarly, a PWM cycle of different regions in each sector is enlarged and displaced, verifying the correctness of the results. Fig. 10(c) shows the PWM signals in the high modulation area (x=4 or 5), and the result of two-fold magnification of the signal S_A is shown in this figure as well. Compared with the traditional SVPWM algorithm, the switching times are reduced by about one-third in the high modulation area.

To verify the correctness and feasibility of proposed PCR method with different carrier frequencies application, the actual and reconstructed currents of the motor with higher 10 kHz and

lower 5 kHz carrier frequencies are recorded, respectively. The current measurement methods are shown in Fig. 8(b), where the actual currents (i_{a_A}, i_{b_A}, i_{c_A}) of the motor are measured by the current clamps, and the reconstructed ones (i_{a_R}, i_{b_R}, i_{c_R}) in the DSP are output by the DAC. The waveforms of i_{a_A}, i_{b_A}, i_{c_A} and i_{a_R}, i_{b_R}, i_{c_R} are consistent. The results are shown in Fig. 11, where the motor speed is 850 r/min under the rated loads. The carrier frequencies of Fig. 11(a) and 11(b) are 10 kHz and 5 kHz, respectively. The current ripple in Fig. 11(a) is smaller, and the voltage utilization in Fig. 11(b) is higher. Reducing the switching frequency does not affect the reconstruction accuracy.

The actual driving performance is affected by the accuracy of the reconstructed currents and the fluctuation of the motor speed. To explore the effect of the errors between the measured and reconstructed currents on the drive performance under different loading conditions, the actual midpoint current (i_{a_M}) and reconstructed current (i_{a_R}) of phase A are compared under no, half, and rated loading conditions. The errors current (i_{erorrs}) and motor speed are obtained, as shown in (a), (b), and (c) of Fig. 12, respectively. The waveforms of i_{a_R} and i_{a_M} are basically coincided in three different loading conditions, and the root mean square (RMS) of i_{errors} is 0.2017A, 0.2671A, and 0.3079A
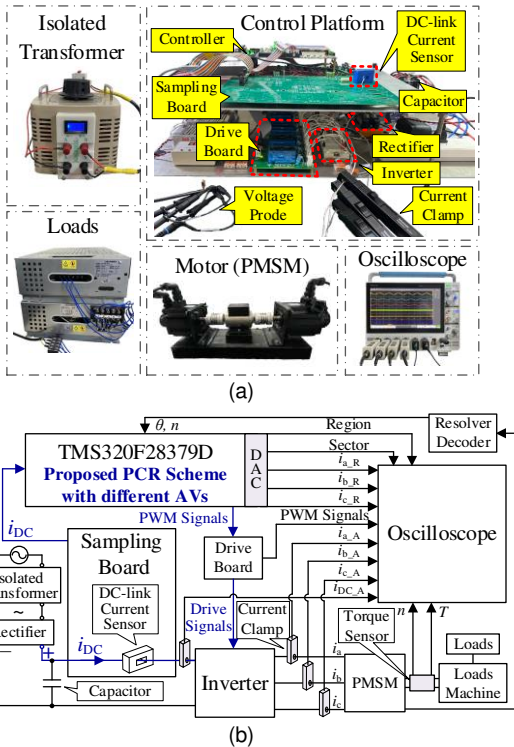

(a)

(b)

Fig. 9. Experimental setup: (a) experimental components, (b) experimental platform architecture.

TABLE VI
MAIN PARAMETERS OF PMSM FOR EXPERIMENT.

Parameters	Value	Parameters	Value
Rated Power	1.0 kW	Line Resistance	1.05 Ω
Rated Voltage	220 V	Line Inductance	2.64 mH
Rated Current	4 A	Rated Speed	2000 rpm
Rated Torque	5 N·m	Pole Pairs	4

Time (4 ms/div)
(a)
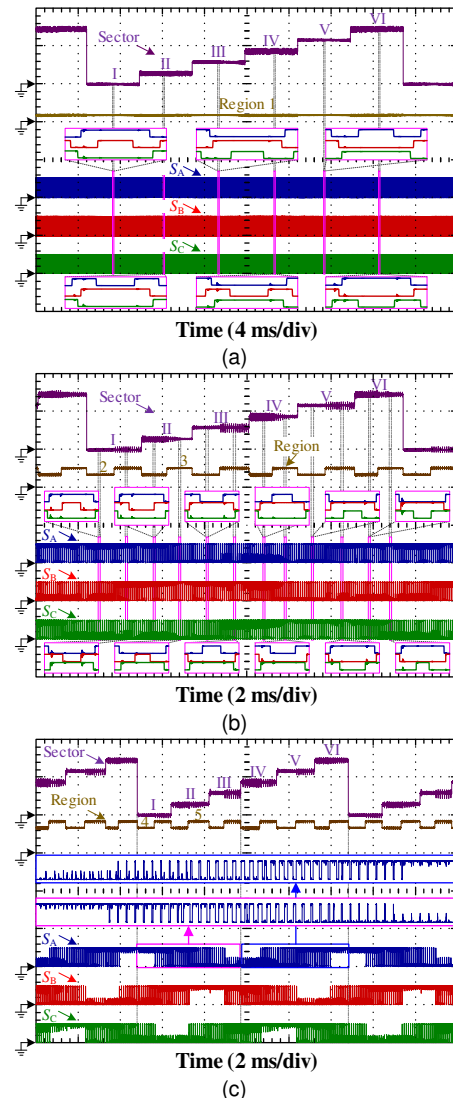

Time (2 ms/div)
(b)

Time (2 ms/div)
(c)

Fig. 10. PWM signals of three modulation areas: (a) in low modulation area, (b) in medium modulation area, and (c) in high modulation area.
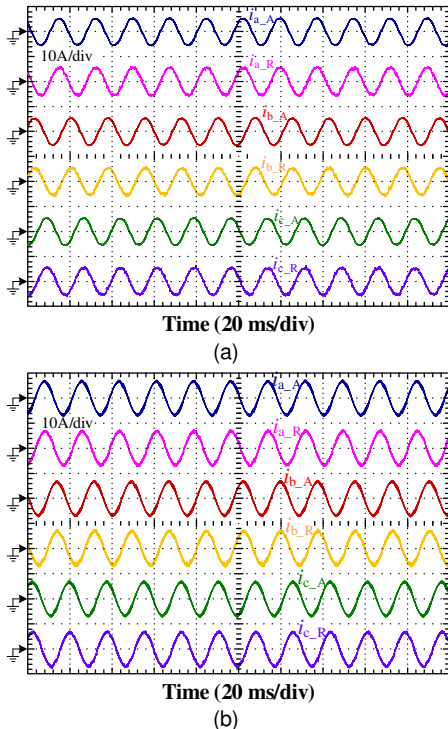
Fig. 11. Actual and reconstructed current waveforms: (a) with 10 kHz carrier frequency, and (b) with 5 kHz carrier frequency.
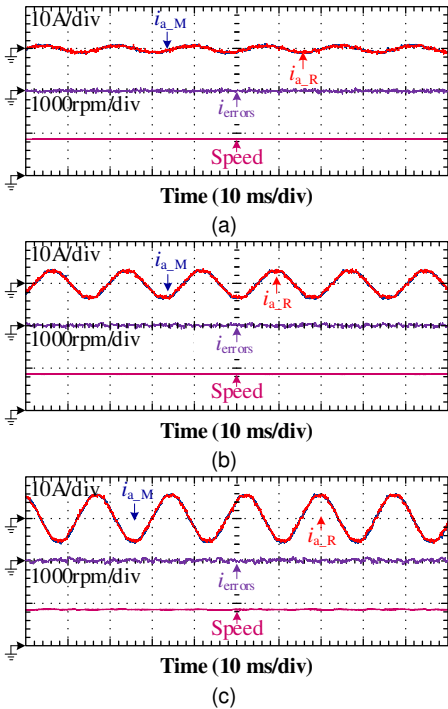

Fig. 12. Waveforms of i_{a_R}, i_{a_M}, i_{errors}, and speed under different loading conditions: (a) at no loading condition, (b) at light loading condition, and (c) at rated loading condition.

under no, light, and rated loading conditions, respectively. i_{errors} decreases as the load decreases. The motor speed is basically stable at 850 rpm. These errors do not have significant impact on the actual drive performance at different loading conditions. The proposed method has no unmeasurable zones in the maximum modulation area. i_{errors} is generated by the measurement errors of current sensor and the sampling errors of current sampling hardware circuit. Besides, these errors may be introduced through the DAC output, therefore, i_{errors} may be smaller than the
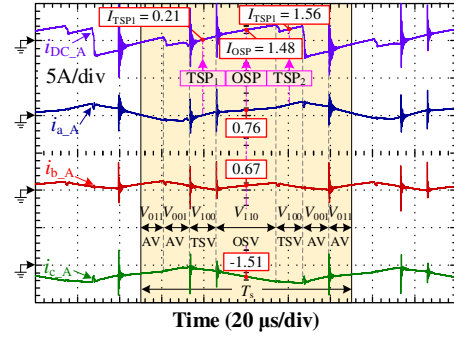

Fig. 13. Waveforms of DC-link current and three-phase currents in region 1 of sector I.

TABLE VII
COMPARISON OF TWO SAMPLING METHODS.

Sampling Method	i_a (A)	Δi_a (A)	i_b (A)	Δi_b (A)
Actual Current	0.76		0.67	
Single Point	0.21	-0.55	1.27	0.60
Proposed	0.89	0.13	0.59	-0.08

one calculated above, and i_{a_R} which is used for closed-loop control may be more precise. Compared with the first method of PCR [13]-[18], although the accuracy of the proposed method is slightly lower, the wiring of this method is simpler and the modulation area does not reduce. Compared with the second method [19]-[29], the proposed method prolongs the duration time of SVs and weakens the influence of time-sharing sampling errors, which hash higher reconstruction accuracy.

When the vector falls into region 1 of sector I and has a value close to 0, the actual DC-link current (i_{DC_A}) and the actual three-phase currents (i_{a_A}, i_{b_A}, i_{c_A}) are shown in Fig. 13. The current waveforms of one PWM cycle are marked with the yellowish shadowed area, where the AVs (V_{011}, V_{001}) and SVs (V_{100}, V_{110}) are used. When TSV (V_{100}) is generated, current samplings are performed on TSP_1 and TSP_2; when OSV (V_{110}) is generated, one sampling is performed on OSP. The average of I_{TSP1} and I_{TSP2} (i_{a_R}) is used to estimate the midpoint current i_{a_A}, I_{OSP} ($-i_{c\_R}$) is used to estimate the midpoint current i_{c_A}, and i_{b_R} is reconstructed by i_{a_R} and i_{c_R}. Compared with the traditional single-point sampling method, the errors of the two methods are shown in TABLE VII. The sampling method of symmetrical points is simple and effective to eliminate the time-sharing sampling errors. In addition, the duration time of the SVs is greater than one-eighth of the cycle, and the DC-link current at the sampling point is relatively stable.

To verify the effect of the proposed method at low speeds, the target speed is set to vary between 50 rpm and 200 rpm (rated speed 2000 rpm). The waveforms of i_{a_A} and speed under different load conditions are given in Fig. 14, where the load is applied at 200 rpm. The motor can run stably at low speed. To verify the range of the maximum modulation area, the speed target is set to the rated speed (2000 rpm), and the waveforms of torque, speed, the actual current i_{a_A}, and the reconstruction currents i_{a_R} are shown in Fig. 15. The rated speed can be reached, and the waveform of i_{a_R} follows i_{a_A} accurately.

To compare the effect of introducing AVs on the current ripple in the capacitor, the motor is driven by the traditional SVPWM method and proposed method, respectively. The DC-link current waveforms for six electrical cycles in different modulation areas are generated by the traditional SVPWM
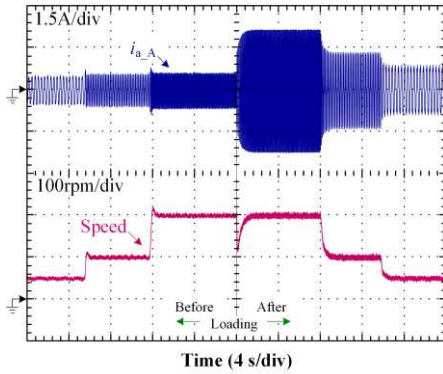
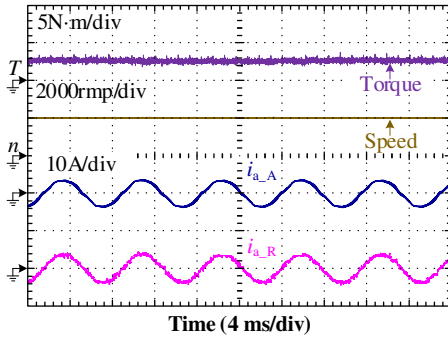Fig. 14. Waveforms of i_{a_A} and speed under different load conditions.

Fig. 15. Waveforms of torque, speed, i_{a_R} and i_{a_A} under 2000 rpm.

Fig. 16. DC-link waveforms of traditional SVPWM method (i_{DC_T}) and proposed reconstruction method (i_{DC_R}): (a) in low modulation area, (b) in medium modulation area, and (c) in high modulation area.

method (i_{DC_T}) and proposed method (i_{DC_R}) respectively, which are shown in (a), (b) and (c) of Fig. 16. The sample standard deviation (SD) is used to measure the magnitude of the ripple. In the low modulation area, the SD of i_{DC_R} and i_{DC_T} is 2.1530 A and 0.9828 A, respectively. In the medium modulation area, the SD of i_{DC_R} and i_{DC_T} is 2.3094 A and 1.5265 A, respectively. In the high modulation area, the SD of i_{DC_R} and i_{DC_T} is 1.1652 A and 1.2933 A, respectively. Larger ripples are generated in low and middle modulation areas with AVs instead of zero vectors. The ripple in the high modulation area is attenuated with AVs.

To compare the efficiency value of the proposed method, the seven-segment SVPWM without AV is chosen. Under the same working conditions, the output power of two methods is equal, and their input power can reflect the difference in efficiency. Therefore, a DC power supply can be used to compare the efficiency of the two methods. The motor is controlled under the same working conditions by two methods, respectively. The output current of the DC power supply is recorded, and the efficiency of the two methods is compared with the output current. The DC power supply provides 310 V DC, and the motor speed in the low, medium and high modulation area is 500, 1000, and 2000 rpm, respectively. The output current of the seven-segment SVPWM method is 0.594 A, 1.386 A, and 2.631 A in the low, medium, and high modulation areas, respectively. The output current of the proposed method is 0.683 A, 1.452 A, and 2.621 A in the low, medium, and high modulation areas, respectively. Because the number of switching times in the low or middle modulation area is larger, the method with AVs is less efficient. However, in the high modulation area, the proposed PCR method of introducing AVs instead of zero vectors is more efficient than the seven-segment SVPWM method.
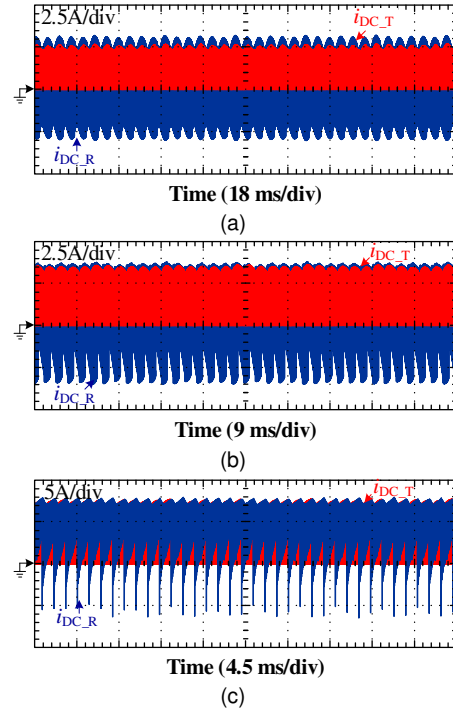
VI. CONCLUSION

To eliminate the unmeasurable zones, T_{min} must be shorter than a harsh T_{limit}, which raises the higher performance requirements on PMSM drive systems. Meanwhile, a shorter T_{limit} limits the generation of symmetrical PWM waves, which makes it unfeasible to use the symmetrical sampling method to eliminate the time-sharing sampling errors. Therefore, the extension of T_{limit} is the key to eliminate the unmeasurable zones and time-sharing sampling errors. To extend T_{limit}, a method is proposed which adopts different AVs for prolonging the duration time of SVs in different regions. The following merits are obtained.

1) A longer T_{limit} (12.5%T_s) allows to relieve the pressure on the hardware of current loop, produces a more stable current waveform during sampling, and improve the sampling accuracy by multiple sampling.
2) The time-sharing sampling errors can be simply eliminated by generating a symmetrical PWM waveform, which can effectively prevent the distortion of the reconstructed current waveforms.
3) The switching times of the inverter can be reduced in the high modulation area, which could greatly reduce the losses of the inverter.

In conclusion, the presented method provides a new solution by modifying the SVPWM algorithm for the PCR technology.

REFERENCES

[1] K. Yu, Z. Wang, X. Wang, and Z. Zou, "An online flux estimation for dual three-phase SPMSM drives using position-offset injection," *IEEE Trans. Power Electron.*, vol. 36, no. 10, pp. 11606-11617, Oct. 2021.
[2] D. Liang, J. Li, R. Qu and W. Kong, "Adaptive second-order sliding-mode observer for PMSM sensorless control considering VSI nonlinearity," *IEEE Trans. Power Electron.*, vol. 33, no. 10, pp. 8994–9004, Oct. 2018.

This article has been accepted for publication in a future issue of this journal, but has not been fully edited. Content may change prior to final publication. Citation information: DOI 10.1109/TIE.2022.3174279, IEEE Transactions on Industrial Electronics

IEEE TRANSACTIONS ON INDUSTRIAL ELECTRONICS

10

[3] Z. Wang, X. Wang, J. Cao, M. Cheng, and Y. Hu, "Direct torque control of T-NPC inverters-fed double-stator-winding PMSM drives with SVM," *IEEE Trans. Power Electron.*, vol. 33, no. 2, pp. 1541–1553, Feb. 2018.

[4] G. Xie, K. Lu, S. K. Dwivedi, J. R. Rosholm and F. Blaabjerg, "Minimum-Voltage vector injection method for sensorless control of PMSM for low-speed operations," *IEEE Trans. Power Electron.*, vol. 31, no. 2, pp. 1785-1794, Feb. 2016.

[5] Z. Zhou, C. Xia, T. Shi, and Q. Geng, "Model predictive direct duty-cycle control for PMSM drive systems with variable control set," *IEEE Trans. Ind. Electron.*, vol. 68, no. 4, pp. 2976–2987, Apr. 2021.

[6] H. Ge, J. W. Jiang, J. Ye and A. Emadi, "Behavior study of permanent magnet synchronous machines based on a new normalized model," *IEEE Trans. Ind. Electron.*, vol. 66, no. 10, pp. 7539-7550, Oct. 2019.

[7] S. Rubino, O. Dordevic, E. Armando, I. R. Bojoi and E. Levi, "A novel matrix transformation for decoupled control of modular multiphase PMSM drives," *IEEE Trans. Power Electron.*, vol. 36, no. 7, pp. 8088-8101, Jul. 2021.

[8] C. Gong, Y. Hu, C. Gan, G. Chen and M. Alkahtani, "Modeling, analysis, and attenuation of uncontrolled generation for IPMSM-based electric vehicles in emergency," *IEEE Trans. Ind. Electron.*, vol. 67, no. 6, pp. 4453–4462, Jun. 2020.

[9] G. Wang, J. Kuang, N. Zhao, G. Zhang, and D. Xu, "Rotor position estimation of PMSM in low-speed region and standstill using zero-voltage vector injection," *IEEE Trans. Power Electron.*, vol. 33, no. 9, pp. 7948–7958, Sept. 2018.

[10] T. M. Wolbank and P. E. Macheiner, "Current-controller with single DC link current measurement for inverter-fed AC machines based on an improved observer-structure," *IEEE Trans. Power Electron.*, vol. 19, no. 6, pp. 1562-1567, Nov. 2004.

[11] B. Saritha and P. A. Janakiraman, "Sinusoidal three-phase current reconstruction and control using a DC-link current sensor and a Curve-Fitting observer," *IEEE Trans. Ind. Electron.*, vol. 54, no. 5, pp. 2657-2664, Oct. 2007.

[12] B. Hafez, A. S. Abdel-Khalik, A. M. Massoud, S. Ahmed and R. D. Lorenz, "Single-Sensor-Based three-phase permanent-magnet synchronous motor drive system with Luenberger observers for motor line current reconstruction," *IEEE Trans. Ind. Appl.*, vol. 50, no. 4, pp. 2602-2613, Jul.-Aug. 2014.

[13] W. Wang, H. Yan, Y. Xu, J. Zou, X. Zhang, W. Zhao, G. Buticchi, and C. Gerada, "New three-phase current reconstruction for PMSM drive with hybrid space vector pulsewidth modulation technique," *IEEE Trans. Power Electron.*, vol. 36, no. 1, pp. 662–673, Jan. 2021.

[14] H. Yan, Y. Xu, W. Zhao, H. Zhang, and C. Gerada, "DC drift error mitigation method for three-phase current reconstruction with single dc hall current sensor," *IEEE Trans. Magn.*, vol. 55, no. 2, pp. 1–4, Feb. 2019.

[15] Y. Xu, H. Yan, J Zou, B. Wang, and Y. Li, "Zero voltage vector Sampling method for PMSM three-phase current reconstruction using single current sensor," *IEEE Trans. Power Electron.*, vol. 32, no. 5, pp. 3797–3807, May 2017.

[16] Y. Cho, T. LaBella, and J. Lai, "A three-phase current reconstruction strategy with online current offset compensation using a single current sensor," *IEEE Trans. Ind. Electron.*, vol. 59, no. 7, pp. 2924–2933, Jul. 2012.

[17] S. Xiao, T. Shi, X. Li, Z. Wang, and C. Xia, "Single-current-sensor control for PMSM driven by quasi-Z-source inverter" *IEEE Trans. Power Electron.*, vol. 34, no. 7, pp. 7013–7024, Jul. 2019.

[18] Q. Tang, A. Shen, W. Li, P. Luo, M. Chen, and X. He, "Multiple-positions-coupled sampling method for PMSM three-phase current reconstruction with a single current sensor," *IEEE Trans. Power Electron.*, vol. 35, no. 1, pp. 699–708, Jan. 2020.

[19] H. Kim and T. M. Jahns, "Phase current reconstruction for AC motor drives using a DC link single current sensor and measurement voltage vectors," *IEEE Trans. Power Electron.*, vol. 21, no. 5, pp. 1413–1419, Sept. 2006.

[20] H. Kim and T. M. Jahns, "Current control for AC motor drives using a single DC-link current sensor and measurement voltage vectors," *IEEE Trans. Ind. Appl.*, vol. 42, no. 6, pp. 1539–1547, Nov./Dec. 2006.

[21] S. Yang, "Saliency-Based position estimation of permanent-magnet synchronous machines using square-wave voltage injection with a single current sensor," *IEEE Trans. Ind. Appl.*, vol. 51, no. 2, pp. 1561–1571, Mar./Apr. 2015.

[22] Y. Gu, F. Ni, D. Yang, and H. Liu, "Switching-state phase shift method for three-phase-current reconstruction with a single DC-link current sensor," *IEEE Trans. Ind. Electron.*, vol. 58, no. 11, pp. 5186–5194, Nov. 2011.

[23] H. Shin and J. Ha, "Phase current reconstructions from DC-link currents in three-phase three-level PWM inverters," *IEEE Trans. Power Electron.*, vol. 29, no. 2, pp. 582–593, Feb. 2014.

[24] W. Lee, D. Hyun, and T. Lee, "A novel control method for three-phase PWM rectifiers using a single current sensor," *IEEE Trans. Power Electron.*, vol. 15, no.5, pp. 861–870, Sept. 2000.

[25] W. Lee, T. Lee, and D. Hyun, "Comparison of single-sensor current control in the DC link for three-phase voltage-source PWM converters," *IEEE Trans. Ind. Electron.*, vol. 48, no. 3, pp. 491–505, Jun. 2001.

[26] J. Ha, "Voltage injection method for three-phase current reconstruction in PWM inverters using a single sensor," *IEEE Trans. Power Electron.*, vol. 24, no.3, pp. 767–775, Mar. 2009.

[27] H. Lu, X. Cheng, W. Qu, S. Sheng, Y. Li, and Z. Wang, "A three-phase current reconstruction technique using single DC current sensor based on TSPWM," *IEEE Trans. Power Electron.*, vol. 29, no. 3, pp. 1542–1550, Mar. 2014.

[28] Y. Lai, Y. Lin, and C. Chen, "New hybrid pulsewidth modulation technique to reduce current distortion and extend current reconstruction range for a three-phase inverter using only DC-link sensor," *IEEE Trans. Power Electron.*, vol. 28, no.3, pp. 1331–1337, Mar. 2013.

[29] J. Lu, X. Zhang, Y. Hu, J. Liu, C. Gan, and Z. Wang, "Independent phase current reconstruction strategy for IPMSM sensorless control without using null switching states," *IEEE Trans. Ind. Electron.*, vol. 65, no. 6, pp. 4492–4502, Jun. 2018.

[30] J. Lu, Y. Hu and J. Liu, "Analysis and compensation of sampling errors in TPFS IPMSM drives with single current sensor," *IEEE Trans. Ind. Electron.*, vol. 66, no. 5, pp. 3852-3855, May 2019.

[31] D. P. Marčetić and E. M. Adžić, "Improved three-phase current reconstruction for induction motor drives with DC-link shunt," *IEEE Trans. Ind. Electron.*, vol. 57, no. 7, pp. 2454–2462, Jul. 2010.

[32] W. Wang, H. Yan, Y. Xu, J. Zou and G. Buticchi, "Improved three-phase current reconstruction technique for PMSM drive with current prediction," *IEEE Trans. Ind. Electron.*, vol. 69, no. 4, pp. 3449-3459, Apr. 2022.

[33] W. Wang, H. Yan, X. Wang, Y. Xu and J. Zou, "Analysis and compensation of sampling-delay error in single current sensor method for PMSM drives," *IEEE Trans. Power Electron.*, vol. 37, no. 5, pp. 5918-5927, May 2022.

[34] J. Im and R. Kim, "Improved saliency-based position sensorless control of interior permanent-magnet synchronous machines with single DC-link current sensor using current prediction method," *IEEE Trans. Ind. Electron.*, vol. 65, no. 7, pp. 5335–5343, Jul. 2018.

[35] J. Ha, "Current prediction in vector-controlled PWM inverters using single DC-link current sensor," *IEEE Trans. Ind. Electron.*, vol. 57, no. 2, pp. 716–726, Feb. 2010.

[36] G. Wang, F. Chen, N. Zhao, Y. Bai, B. Li, S. Liu, and D. Xu, "Current reconstruction considering time-sharing sampling errors for single DC-link shunt motor drives" *IEEE Trans. Power Electron.*, vol. 36, no. 5, pp. 5760–5770, May 2021.

[37] M. Gu, S. Ogasawara and M. Takemoto, "Novel PWM schemes with multi SVPWM of sensorless IPMSM drives for reducing current ripple," *IEEE Trans. Power Electron.*, vol. 31, no. 9, pp. 6461–6475, Sept. 2016.

Yuge Song was born in Shaanxi, China, in 1998. She received the B.S. degree in electrical engineering from Northwest Agriculture and Forestry University, Yangling, China, in 2020. She is currently working toward the Ph.D. degree in electrical engineering, Northwestern Polytechnical university, Xi'an, China.

Her research interests include motor drivers, power electronics, and calibration of sensors in permanent magnet synchronous motor drives.
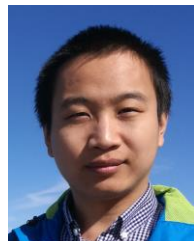
Jiadong Lu (Senior Member, IEEE) was born in Pucheng, China, 1990. He received the B.S., the M.S. and the Ph.D. degrees in electrical engineering from Northwestern Polytechnical University (NWPU), Xi'an, China in 2012, 2015 and 2018, respectively. Between 2017 and 2018, he was with the Department of Electrical Engineering, Electronics and Computer Science, University of Liverpool (UoL), U.K. as an Honorary Academic Researcher. Currently, he is an Associate Research Fellow at the Department of Electrical Engineering, NWPU.

His research interests include hybrid-fault-tolerant control techniques for permanent magnet synchronous motor drives, aging issue for motor drives and power electronics converters & control.

Yihua Hu (Senior Member, IEEE) received the B.S. degree in electrical engineering in 2003, and the Ph.D. degree in power electronics and drives in 2011, both at China University of Mining and Technology. Between 2011 and 2013, he was with the College of Electrical Engineering, Zhejiang University as a Postdoctoral Fellow. Between 2013 and 2015, he worked as a Research Associate at the power electronics and motor drive group, the University of Strathclyde. Between 2016 and 2019, he was a Lecturer at the Department of Electrical Engineering and Electronics, University of Liverpool (UoL). Currently, he is a reader at Electronics Engineering Department at University of York (UoY). He has published 85 papers in IEEE Transactions journals. His research interests include renewable generation, power electronics converters & control, electric vehicle, more electric ship/aircraft, smart energy system and non-destructive test technology. He is the associate editor of IEEE Transactions on Industrial Electronics, IET Renewable Power Generation, IET Intelligent Transport Systems and Power Electronics and Drives.

Wei Zhang received the B.S. degree in marine electrical and electronics engineering from Dalian Maritime University, Dalian, China, in 2021. He is currently pursuing the M.S. degree in electrical engineering, Northwestern Polytechnical university, Xi'an, China. His research interests include motor drivers, power electronics, and integrated chargers on electric vehicles.

Yue Su received the B.S. degree in electrical engineering and automation from China University of Petroleum (East China), Qingdao, China, in 2015. He is currently working toward the M.S. degree in electrical engineering at Northwestern Polytechnical University, Xi'an, China. His research interests include fault-tolerant control techniques for permanent magnet synchronous motor drives and power electronics converters.

Xuyang Wu received the B.S. degree in marine electrical and electronics engineering from Dalian maritime University, Dalian, China, in 2021. He is currently pursuing the M.S. degree in electrical engineering, Northwestern Polytechnical university, Xi'an, China. His research interests include permanent magnet synchronous motor drives, calibration of sensors in permanent magnet synchronous motor drives and power electronics.

Jinglin Liu (Member, IEEE) received the B.Eng. degree in electrical engineering from Tsinghua University, Beijing, China, in 1986, and the M.Eng. and the Ph.D. degrees in electrical engineering from NWPU, Xi'an, China, in 1990 and 2002, respectively. Since 1994, he has been a Faculty Member with NWPU, Xi'an, where he is currently a Professor of Electrical Engineering. His research interests include electrical machines design and drives, power electronics, fault diagnosis, and motion control.